 doi:10.20944/preprints202010.0183.v1

Article

Structural origin of magnetotransport properties in APCVD deposited single and bi-layer tin oxide thin films

Krunoslav Juraić [1,*], Matija Čulo [2,3], Željko Rapljenović [2], Jasper Rikkert Plaisier [4], Zdravko Siketić [1], Luka Pavić [1], Mario Bohač [1], Aden Hodzic [5], Davor Gracin [1]

[1] Ruđer Bošković Institute, Bijenička cesta 54, 10000 Zagreb, Croatia
[2] Institute of Physics, Bijenička cesta 46, 10000 Zagreb, Croatia
[3] High Field Magnet Laboratory (HFML-EMFL) Institute for Molecules and Materials, Radboud University, Toernooiveld7, 6525 ED, Nijmegen, Netherlands
[4] Elettra - Sincrotrone Trieste S.C.p.A., SS 14, km 163.5, Basovizza (TS), Italy
[5] Central European Research Infrastructure Consortium, Strada Statale 14, km 163.5, 34149, Basovizza, TS, Italy

* Correspondence: kjuraic@irb.hr; Tel.: +385-1- 456-0970 (K.J.)

Abstract: Tin oxide (SnO_2) thin films, undoped single-layer and fluorine doped / undoped bilayer were deposited by Atmospheric Pressure Chemical Vapour Deposition (APCVD) at soda-lime glass substrate at two different temperatures (590°C and 610°C). Transport properties examined by impedance spectroscopy, DC resistivity, Hall effect and magnetoresistance measurements are correlated with structural properties examined by Scanning Electron Microscopy, Grazing Incidence X-ray Diffraction (GIXRD) and Time-of-flight Elastic Recoil Detection Analysis (TOF-ERDA). Results suggest that charge transport in the obtained samples is dominated by scattering at neutral impurities and can be correlated with preferred orientation (texture coefficient) presented in prepared samples.

Keywords: tin oxide, thin films, atmospheric pressure chemical vapour deposition transport properties, magnetoresistance, impedance spectroscopy, charge carrier mobility

1. Introduction

Transparent conductive oxides (TCO) are binary or ternary compounds containing one or two metallic elements. TCO materials are characterized by a very good balance of optical and electrical properties. Widely used TCO are oxides such as ZnO, SnO_2, In_2O_3 doped with metallic elements: Al-doped ZnO (AZO), Sn-doped In_2O_3 (ITO) and F-doped SnO_2 (FTO) [1–3].

Among others, tin oxide (SnO_2), also known as stannic oxide, is an n-type semiconductor (due to oxygen vacancies) with high optical transparency in visible spectral range (> 85%) and wide energy band gap (3.6 eV). It can be found in nature as a mineral known as cassiterite, and it is the main ore of tin [4]. It has a rutile-like crystal structure. The SnO_2 thin films are chemically inert, scratch resistant, and can withstand high temperatures [5].

SnO_2 thin films (pure and doped) have various applications in devices used in daily life: solar energy conversion, flat panel displays, electro-chromic devices, invisible security circuits, LEDs, transparent electrical conductors and non-colouring electrodes, in smart windows, for energy and illumination control, in anti-dazzling rear view windows, and non-emissive displays, low-emittance coatings for energy efficient windows, anti-frost coatings on car windows and transparent electrode for solar cells. In these applications the film thickness normally lies in the 100–1000 nm range [5].

For photovoltaic application (as transparent front electrode) it is important that SnO_2 is transparent for UV-VIS light and has very good conductivity at the same time. Electrical conductivity can be improved by increasing charge carrier density (doping with foreign atoms) or

 doi:10.20944/preprints202010.0183.v1

charge carrier mobility. The most favourable dopants are antimony (SnO_2:Sb) and fluorine (SnO_2:F). Fluorine doped tin oxide (SnO_2:F, FTO) exhibits good visible transparency owing to its wide band gap, while retaining a low electrical resistivity due to the high carrier concentration caused by the oxygen vacancies and the fluorine dopant. Higher number of charge carriers causes lower film transparency. Therefore, better conductivity should be achieved by optimizing carrier mobility. Several different approaches are reported how to improve mobility of SnO_2 such as post-deposition heat treatment, deposition technique, substrate, doping control[7]. For example, mobility can be improved by use of highly oriented substrate, use of tin tetrachloride as Sn precursor, higher methanol content.

There are various chemical and physical methods for preparation of pure and doped SnO_2 thin films: chemical vapour deposition, sol gel, spray pyrolysis, electron beam evaporation, vapour deposition, pulsed laser deposition, molecular beam epitaxy, thermal evaporation, reactive evaporation and magnetron sputtering, reactive magnetron sputtering, ion beam deposition [5].

In this work Atmospheric Pressure Chemical Vapour Deposition (APCVD) was used for SnO_2 thin films deposition. APCVD is a process which enables deposition of vapour species into thin solid films via suitable chemical reactions at atmospheric pressure. By careful choice of the deposition parameters the film properties can be systematically targeted. APCVD is often used in industry for thin film coatings deposition because of reduced costs due to low material consumption, high deposition rates and running costs (compared to low pressure systems) [6].

In our previous publication [8], we reported in detail about structural properties examined by XRD of SnO_2 thin film samples deposited by APCVD with a short discussion about the influence on optical (average transmittance in VIS part of the spectrum) and transport properties (specific surface resistivity). In this work, we have investigated in more detail the transport properties of APCVD deposited SnO_2 thin films and corelated with structural properties. We present how a very small variation in APCVD deposition temperature results in significantly different transport properties (charge carrier mobility). We explain these differences by variation in structural properties (mainly preferred nanocrystal orientation). For this purpose, we prepared undoped SnO_2 thin film single-layer samples and undoped / fluorine-doped SnO_2 (SnO_2:F) bilayer thin films at two different temperatures (590°C and 610°C). Transport properties were examined in a wide temperature range by impedance spectroscopy, DC resistivity, Hall effect and magnetoresistance. Structure and composition of SnO_2 thin films were examined by Scanning Electron Microscopy (SEM), Grazing Incidence X-ray Diffraction (GIXRD) and Time-of-flight Elastic Recoil Detection Analysis (TOF-ERDA).

2. Materials and Methods

2.1. Thin film deposition by APCVD

SnO_2 thin film samples were prepared by the APCVD on the soda-lime glass substrate, in an industrial moving belt reactor [9] with constant-temperature zones. The reactor oven is interrupted with 2 slots perpendicular to the belt moving directions supplied with setup with nozzle that enable the vapour or reactants flow onto the heated glass surface. The reacting gas mixture was $SnCl_4$, H_2O, methanol and oxygen for undoped films while for doped films methanol was omitted and the freon gas was added into the vapour mixture. The vapour of reactants was produced in a "bubbler" by passing a carrier gas through the precursors at room temperature (methanol) or moderately heated to 50°C ($SnCl_4$) or 40°C (H_2O). The carrier gas for $SnCl_4$, ethanol and H_2O was nitrogen. The temperature of glass substrate before and after deposition was 590°C for one series of samples and 610°C for other. The glass substrates were loaded by a belt into the furnace for SnO_2 layer deposition. Single-layer deposition duration of 1.5 minutes and post-deposition thermal treatment of some 30 minutes were adjusted by the belt speed. SnO_2 film is formed through the very fast reaction of tetrachloride with water vapour and methanol is often added as a moderator. That is why for doped samples where the methanol is omitted, the growth rate is some 30% faster that is similar to the result reported in ref.[10].

Preprints (www.preprints.org) | NOT PEER-REVIEWED | Posted: 8 October 2020 doi:10.20944/preprints202010.0183.v1

Table 1. Deposition parameters for SnO_2 thin film samples: sample labels, sample type (single-layer or bilayer), deposition temperature and layer thickness.

Sample label	Sample type	Deposition temperature	Thickness (nm)
S-590	single-layer	590°C	390
S-610	single-layer	610°C	300
B-590	bi-layer	590°C	920
B-610	bi-layer	610°C	710

As a result, two types of films were prepared. The first type was created in a single-step process and the produced samples were intrinsic. The second type was prepared by depositing the first layer on the glass substrate in the same way as for the first type while the second (top) layer, which was formed from the solution without methanol and with addition of fluorine atoms in the form of freon (Chlorofluorocarbon, CFC), was deposited on the already formed first layer.

2.2. Structural characterization

2.2.1. Scanning Electron Microscopy (SEM)

Sample surface morphology was analysed using JEOL, JSM 7000F field emission scanning electron microscope (FE-SEM). Used image acquisition conditions were: 5kV, 10mm working distance, magnification 25k.

2.2.2. Grazing Incidence X-ray Diffraction (GIXRD)

As-deposited films were thoroughly studied by GIXRD, using the synchrotron radiation source. GIXRD was carried out at the MCX beamline [11] (Elettra synchrotron, Trieste, Italy) with the wavelength of the incident beam of 1.5498 Å (8 keV). The angle of incidence was set to 2.0° (value much higher than the critical angle for total external reflection for SnO_2 $\alpha_c = \sqrt{2\delta} \approx 0.37°$, calculated from SnO_2 index of refraction, real part δ [12]). For the critical angle, the beam penetrates 10-20 nm below the surface and gives information about the surface morphology. For the angle of incidence α_i = 2.0° the beam penetrates much deeper and the GIXRD pattern contains the morphological information for the entire SnO_2 layer.

2.2.3. Time-of-flight Elastic Recoil Detection Analysis (TOF-ERDA)

Atomic content and depth profiles of the elements in the samples were determined using TOF-ERDA. TOF-ERDA measurements were done by 20 MeV $^{127}I^{6+}$ ions with 20° incidence angle toward the sample surface, and TOF-ERDA spectrometer positioned at the angle of 37.5° toward the beam direction. More details about TOF-ERDA setup used in this work can be found in ref. [13].

2.3. Transport characterization

2.3.1. Impedance spectroscopy

Sheet conductivity of SnO_2 thin film samples was measured by impedance spectroscopy (Novocontrol Alpha-N dielectric analyser) in the frequency range from 0,01 Hz to 1 MHz, in three subsequent temperature cycles: *i)* cooling from 20 °C to -100 °C, *ii)* heating from -100 °C to 220 °C, *iii)* cooling from 220 °C to 20 °C. Temperature step for all cycles was 40 °C. Sheet conductivity data were normalized to the film thickness (Table 1) to obtain specific conductivity (S/cm).

2.3.2. Magnetotransport

Preprints (www.preprints.org) | NOT PEER-REVIEWED | Posted: 8 October 2020 doi:10.20944/preprints202010.0183.v1

DC resistivity ϱ, magnetoresistance and Hall effect measurements were done in the temperature interval from 4 to 300 K and in magnetic fields up to 5 T. Thin film samples were cut for the Hall-bar geometry with typical dimensions (10mm x 2mm x 500nm). Two current contacts and three pairs of Hall contacts were made by applying silver paint directly to the surface of the films. Magnetoresistance and Hall effect were measured simultaneously at fixed temperatures and magnetic field, B, going from -5 to 5 Tesla. Magnetic field was oriented perpendicular to the current through the sample and perpendicular to the surface of the films. Magnetoresistance data was symmetrized, $V_{xx} = \frac{V_{xx}(+B)+V_{xx}(-B)}{2}$ (V_{xx} is the measured voltage), in order to eliminate the possible mixing of the Hall component and the Hall signal was antisymmetrized, $V_{yx} = \frac{V_{yx}(+B)-V_{yx}(-B)}{2}$, in order to eliminate the possible mixing of the magnetoresistance component. Hall resistance $R_{yx} = V_{yx}/I$ was linear in magnetic field B in the whole temperature range for all samples and the Hall coefficient was obtained as $R_H = \frac{V_{yx}\,t}{I\,B}$, where I is the current and t the sample thickness. The magnetoresistance was standardly determined as $\frac{\Delta\rho}{\rho_0} = \frac{\rho(B)-\rho(0)}{\rho(0)}$.

3. Results and discussion

3.1. Structural properties

3.1.1. Scanning Electron Microscopy

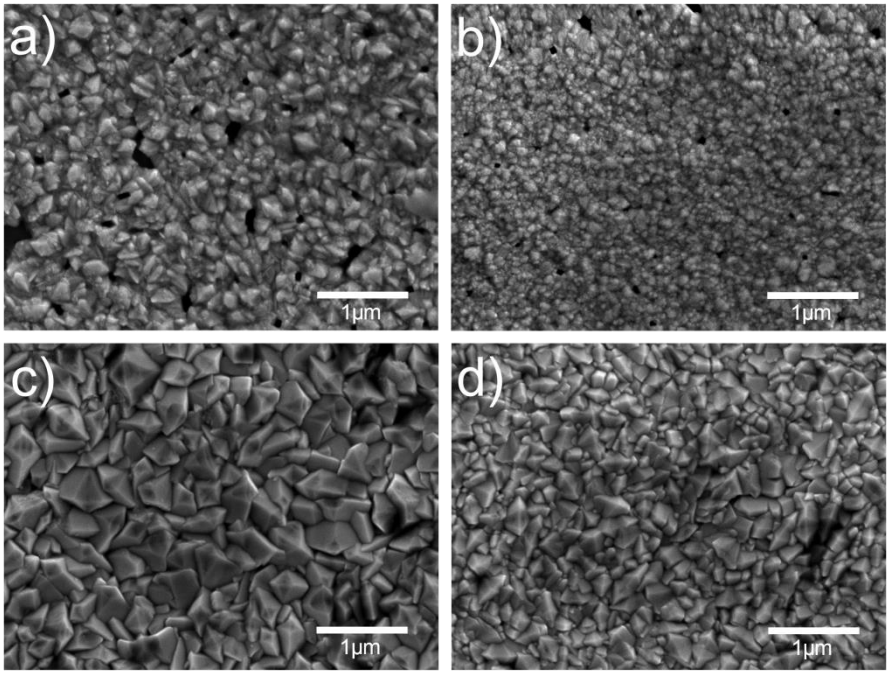

Figure 1 SEM images of SnO_2 single-layer and bi-layer samples: a) S-590, b) S-610, c) B-590 and d) B-610. Average grain size calculated using Eq. (1) are: 104nm (S-590), 84 nm (S-610), 190nm (B-590), 99nm (B-610).

In Figure 1 SEM images of SnO_2 thin film samples are presented. Average grain size was calculated from SEM image line profiles using so called "linear intercept technique" as[14] :

$$\bar{D} = 1.56\frac{C}{MN} \quad (1)$$

where C is a total length of test line used, N is the number of intercepts and M is the SEM image magnification.

There is a significant difference in surface morphology (grain size and shape) for undoped single-layer samples (Figure 1a and 1b) and bi-layer samples (Figure 1c and 1d). Bi-layer samples

Preprints (www.preprints.org) | NOT PEER-REVIEWED | Posted: 8 October 2020 doi:10.20944/preprints202010.0183.v1

have larger grains with sharp edges (pyramidal shape), while single-layer samples have smaller grains with a more rounded shape. The single-layer samples were deposited with addition of methanol just as it was done in experiment reported in refs. [10,15,16] which resulted in smoother films with smaller grains and a higher nucleation density as reported in ref.[15,16]. This effect was addressed to the removal of absorbed HCl which is produced during deposition in reaction of $SnCl_4$ with H_2O. Removal of absorbed HCl leads to an increase in number of adsorption sites for $SnCl_4$ and H_2O, and consequently an increase in the micro-grain density and simultaneously decrease of grain size.

Higher deposition temperature produces samples with smaller grains (surface roughness) for both single-layer and bi-layer samples. This effect could be a result of competing gas-phase and/or surface reactions, which are a complex function of temperature and composition of reactants [17].

3.1.2. Grazing Incidence X-ray Diffraction

Figure 2 shows GIXRD patterns of the single-layer and bi-layer SnO_2 thin film samples recorded at the fixed value of incident angle 2.0°. All observed reflections are unambiguously assigned to the tetragonal structure of SnO_2 (space group $P4_2/mnm$, SnO_2 COD database ID: 9009082 [18]), mineralogical name cassiterite). XRD peaks (Figure 2) are fitted to PseudoVoight peak profiles.

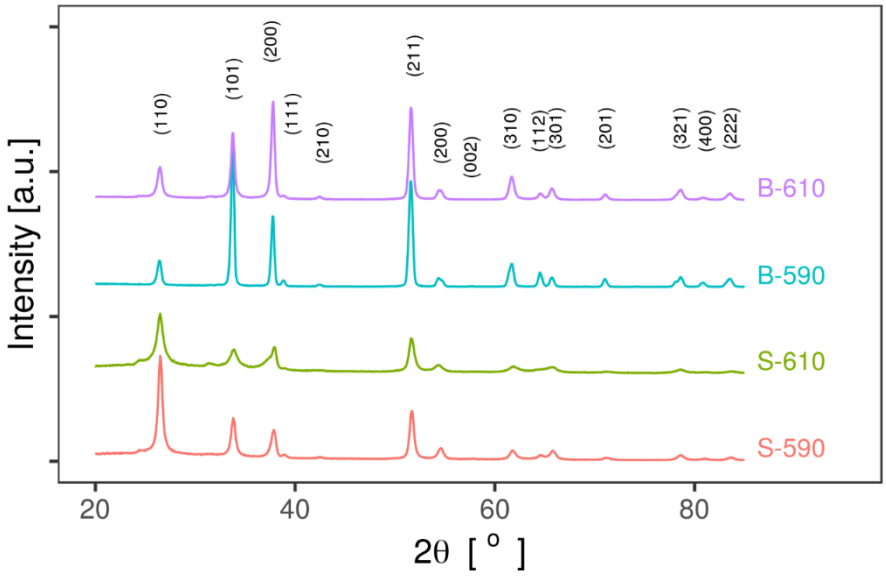

Figure 2 GIXRD diffractograms for single-layer and bi-layer SnO_2 thin film samples. All visible peaks are indexed and labeled.

Table 2 Result of GIXRD analysis: lattice parameters (a, c), texture coefficients for four most intense peaks (calculated using Eq. 2), average maximum microstrain and average nanocrystal size (calculated using Eq. 3).

sample	Lattice parameters		Preferred orientation Texture coefficient				Average maximum microstrain $e \cdot 10^{-3}$	Average nanocrystal size [nm]
	a [nm]	c [nm]	(110)	(101)	(200)	(211)		
S-590	0.474(9)	0.318(4)	0.144	0.090	0.104	0.151	5 ±2	18 ± 3
S-610	0.475(7)	0.318(8)	0.143	0.101	0.140	0.136	10 ±10	14 ± 5
B-590	0.475(9)	0.318(7)	0.019	0.141	0.102	0.166	4 ± 3	24 ± 5

Preprints (www.preprints.org) | NOT PEER-REVIEWED | Posted: 8 October 2020 doi:10.20944/preprints202010.0183.v1

B-610	0.475(7)	0.318(5)	0.031	0.087	0.173	0.159	4 ± 2	21 ± 4

Lattice parameters calculated from peak positions (labelled in Figure 2) are presented. Compared to values from literature (a=0.4737(3) nm and c=0.3186(4) nm) all samples have a larger value of the lattice parameter, a, and equal lattice parameter, c. Variations of lattice parameters are due to the presence of intentional (flour) and non-intentional (chlorine) dopant atoms with different ionic radius which substitute oxygen atoms in the lattice.

There is also a significant variation in XRD peak intensity ratio from sample to sample which are also different from values expected from literature. This suggests the presence of preferred orientation (texture) in films. For quantitative analysis the texture coefficient for a selected XRD peak was calculated as intensity ratio of the selected XRD peak and the total sum of all fitted XRD peaks using the formula[19,20]:

$$TC(h,k,l) = \frac{I(hkl)/I_0(hkl)}{\frac{1}{N}\sum_1^N I(hkl)/I_0(hkl)} \quad (2)$$

where I(h,k,l) is the measured relative intensity of the plane (h k l), I_0(h k l) is the standard intensity of the plane (h k l) taken from literature (COD database, SnO_2 COD ID: 9009082 [18]) and N is the number of reflections included in the calculations. Results for four most intense XRD peaks are presented in Table 2. It is interesting that samples deposited at lower temperature (both single and bilayer) have significantly larger texture coefficient for (110) while bi-layer samples have larger (200) texture coefficient.

Nanocrystal size and average maximum microstrain were determined by fitting the data to the standard Williamson-Hall model (Figure 4)[21]:

$$\beta_{hkl}\cos\theta = \frac{K\lambda}{D} + 4\epsilon\sin\theta \quad (3)$$

where β_{hkl} is XRD line width, D is nanocrystal size, K is shape factor (0.94) and λ (=0.154nm) is the wavelength of Cu K-α radiation. Williamson - Hall model assumes that the broadening of XRD pattern is attributed to the nanocrystal size-induced or strain induced broadening. Assuming that the nanocrystal size and strain contributions to the line broadening are independent to each other, the observed line breadth is simply the sum of the two independent contributions given by Eq. (3).

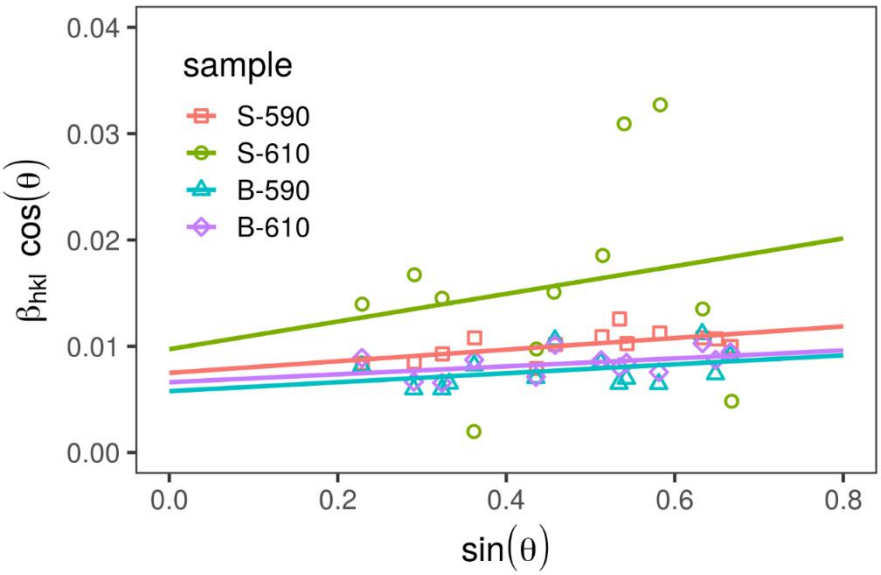

Figure 3 Williamson-Hall plot for SnO_2 samples. Linear fits to data are added.

The values for average nanocrystal size and average maximum microstrain obtained by Williamson-Hall analysis are presented in Table 2.

Preprints (www.preprints.org) | NOT PEER-REVIEWED | Posted: 8 October 2020 doi:10.20944/preprints202010.0183.v1

Single-layer samples have smaller nanocrystal size calculated from GIXRD and clearly seen from SEM images. Two possible effects/reasons can be responsible for smaller nanocrystal size in single-layer samples. First is smaller thickness of single-layer samples which assume smaller nanocrystals at the surface according to standard thin film growth model [22]. The second one is variation in the deposition temperature. Samples deposited at the lower temperature have larger average nanocrystal size. Temperature affects a complicated set of chemical reaction during the mixing of reactants in vapour phase and at the substrate surface.

3.1.3. TOF-ERDA

TOF-ERDA was employed for the elemental depth profiling of the S-590 and B-590 samples. Due to the overlapping of Sn and scattered I lines in TOF-E spectra (Figure 4a and 4Figure 4b), only first $1000 \cdot 10^{15}$ at./cm^2 of sample depth was analysed. Energy spectra belonging to each element were analysed using simulation code Potku [23] (slab analysis) and Monte Carlo (MC) code CORTEO [24]. Calculated depth profiles (Potku analysis) are presented at Figure 5a and 5b for S-590 and B-590 respectively. Since the slab analysis does not take into account detector energy resolution and all other contributions to the total energy spread (energy straggling and multiple scattering of incoming and recoiled ions), derived atomic concentrations were used only as an input data for the MC simulation. Average atomic concentrations, calculated by MC simulations, are listed in the Table 3.

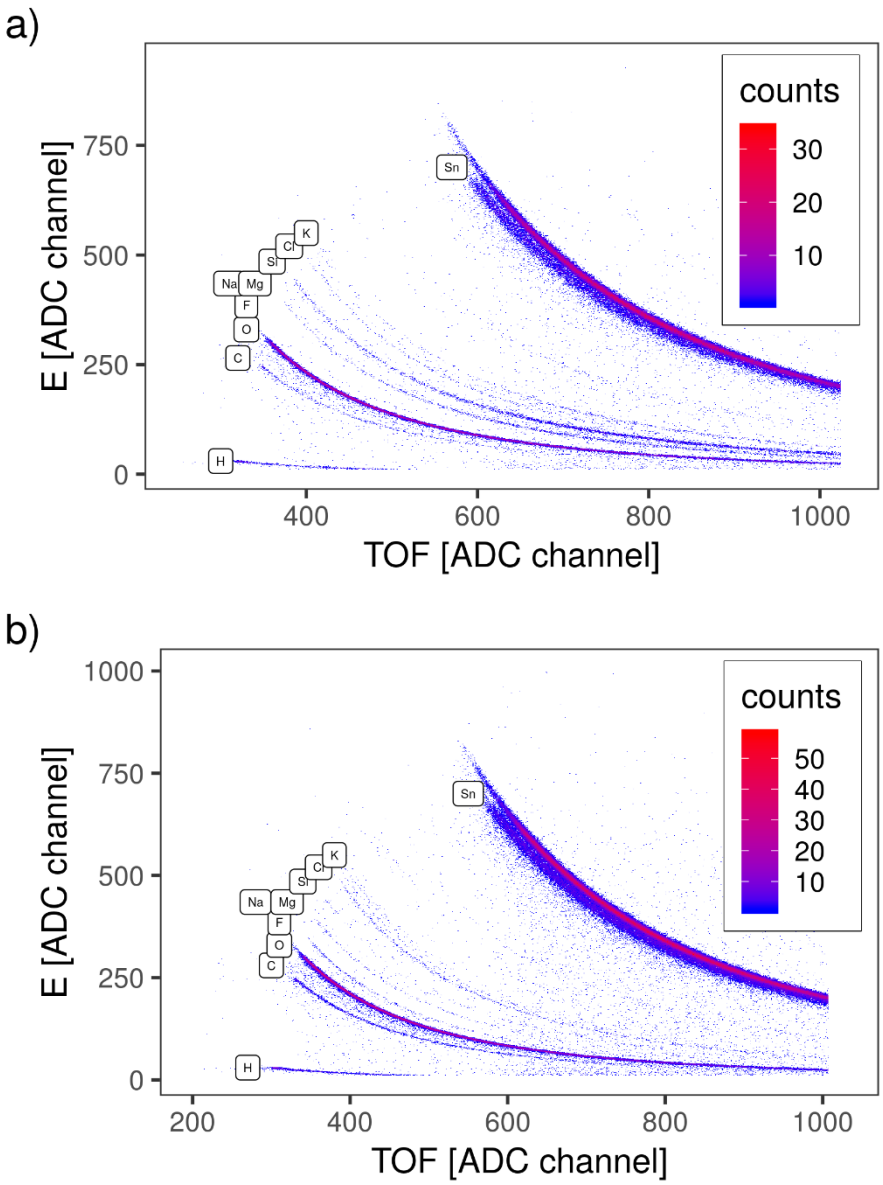

Preprints (www.preprints.org) | NOT PEER-REVIEWED | Posted: 8 October 2020 doi:10.20944/preprints202010.0183.v1

Figure 4 TOF-E map for: a) single-layer (undoped) SnO_2 sample (S-590) and b) bi-layer (undoped + F-doped) SnO_2 sample (B-590)

Table 3 Summary of TOF-ERDA elemental analysis (MC simulation). Total atomic content is normalized to 100%.

SAMPLE	H (at.%)	C (at.%)	O (at.%)	F (at.%)	Na (at.%)	Mg (at.%)	Si (at.%)	Cl (at.%)	K (at.%)	Sn (at.%)
S-590	2.8±0.3	1.7±0.2	62±4	-	0.6±0.1	0.18±0.06	1.8±0.2	0.7±0.1	0.25±0.06	29±2
B-590	2.9±0.3	3.2±0.3	62±4	0.9±0.1	0.26±0.06	0.03±0.02	0.11±0.03	0.9±0.1	0.3±0.1	29±2

The results in Table 3 confirm that undoped single-layer sample (S-590) does not contain flour, as it is expected.

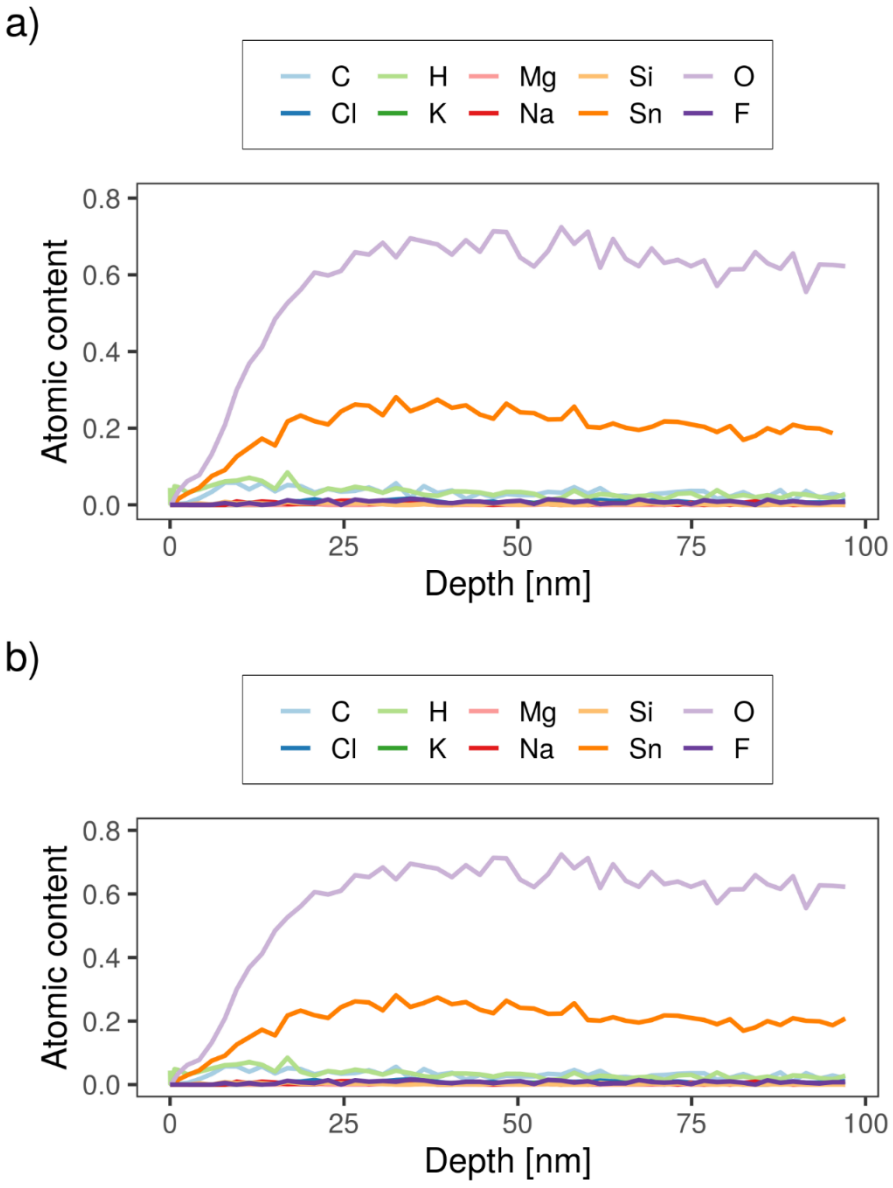

Preprints (www.preprints.org) | NOT PEER-REVIEWED | Posted: 8 October 2020 doi:10.20944/preprints202010.0183.v1

Figure 5 TOF-ERDA elemental depth profile calculated by Potku (slab analysis) for a) single-layer (S-590) and b) bi-layer (B-590) samples deposited at 590 °C

For both samples, ratio of Sn and O atoms are stochiometric (1:2), within the measured error, considering that part of O atoms are bonded to Si in substrate or C atoms at the sample surface. For doped bi-layer samples concentration of F atoms (dopant) is almost 1% while for undoped sample the amount of F atoms is below detection limit (<0.1 at. %).

Small amount of Si, K, Mg and Na, visible in TOF-E spectra (Figure 4a and 4b), could originate from the glass substrate since the sample area is not fully covered by SnO_2 film. Higher number of holes/cracks is expected for thinner samples (single-layer) which could explain higher contribution of Si, K, Mg and Na in the sample S-590 (Table 3).

3.2. Transport properties

3.2.1. Impedance spectroscopy

Impedance spectroscopy results (Figure 6) show that all samples have a very high electrical conductivity, independent of frequency in a wide frequency range indicating fast electronic transport. As expected, bi-layer samples have higher conductivity compared to single-layer deposited at the same temperature because of doping. Only sample S-590 shows a very small dispersion at the highest frequencies. In addition, for all samples the electrode polarisation effects are not observed, indicating the absence of ion transport contribution to the electrical conductivity.

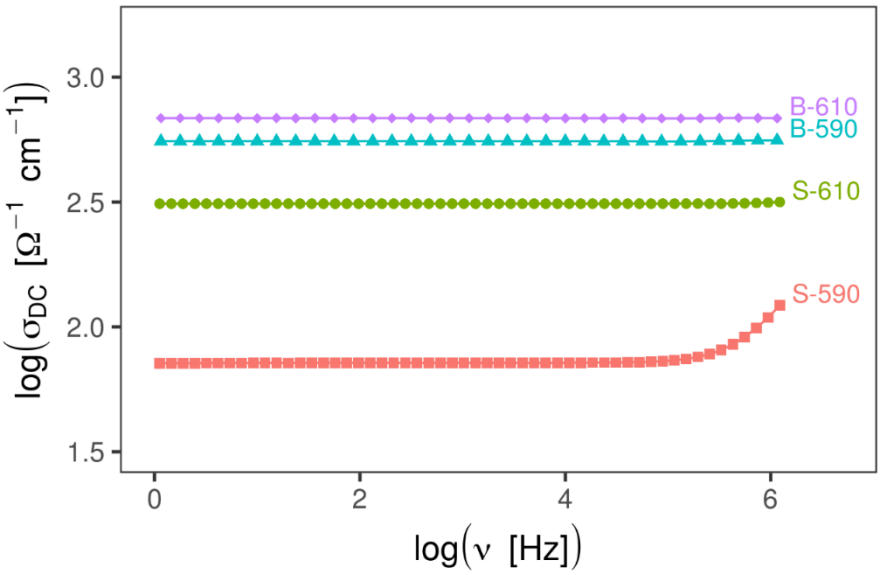

Figure 6 Electrical conductivity as a function of frequency at 20ºC for all SnO_2 samples.

3.2.2. Magnetotransport probe

DC resistivity (Figure 7) for all samples (single-layer and bi-layer) is practically temperature-independent in a wide temperature range up to the room temperature (4-300K) indicating that the Fermi level is either in the conductive band or in the region where the conductive band is mixed with impurity levels. As well, above room temperature resistivity is independent on temperature and have same trend as below room temperature. Temperature independent resistivity shows that we have a metal type of conductivity, but the dominant scattering is not on phonons but on neutral defects. Namely, only the scattering on neutral impurities is temperature independent, and all other scatterings has the same temperature dependence.

Figure 7 clearly shows that undoped samples S-590 and S-610 have greater resistivity than the doped samples B-590 and B-610. This is in line with expectations. There is a small difference in

Preprints (www.preprints.org) | NOT PEER-REVIEWED | Posted: 8 October 2020 doi:10.20944/preprints202010.0183.v1

resistivity between the two undoped samples and also between the two bi-layer (doped) samples. This can be explained by slightly different deposition conditions (temperature).

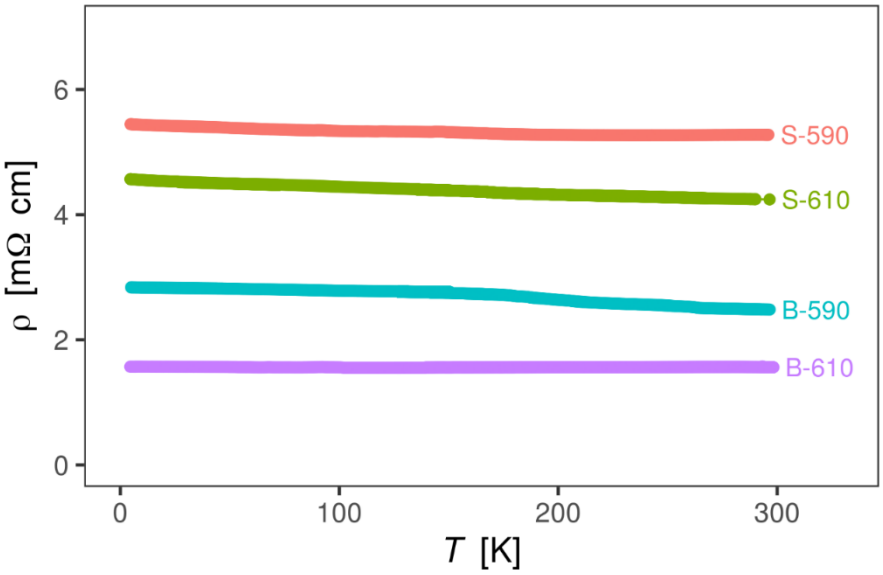

Figure 7 Resistivity of SnO_2 single-layer and bi-layer samples deposited at 590 and 610°C.

Figure 8 shows the temperature dependence of the Hall coefficient R_H for all four samples. R_H is almost temperature independent which is typical for metallic systems showing again that the Fermi level is positioned in the conductive band or in the part where the conductive band and impurity levels are mixed. R_H is negative for all samples, meaning that the dominant charge carriers are electrons in accordance with intrinsic and extrinsic doping.

Undoped samples (S-590 and S-610) have a higher R_H in absolute terms, i.e. they have lower number of charge carriers than doped samples (B-590 and B-610) which is in line with expectations. The small differences between the two undoped, as well as between the two doped samples (Figure 8) are essentially within the error bars in a wide temperature range.

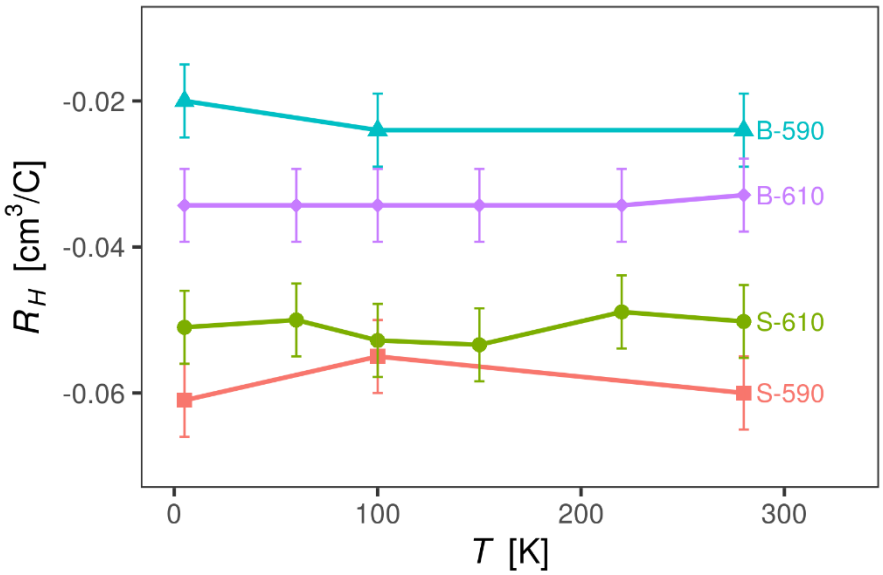

Figure 8 Hall coefficient R_H for SnO_2single-layer and bi-layer samples in the temperature range 4 - 300 K

Magnetoresistance (Figure 9) of all samples is small (< 2 %) and negative and its value slowly increases with cooling. Negative magnetoresistance is rare in non-magnetic materials and usually

Preprints (www.preprints.org) | NOT PEER-REVIEWED | Posted: 8 October 2020 doi:10.20944/preprints202010.0183.v1

has an exotic origin indicating again that SnO_2 samples do not follow simple metallic behavior. However, negative magnetoresistance is found in impurity conduction of many semiconductors[25–27] and is often attributed to specific mechanisms of scattering on disorder which is in accordance with the conclusions extracted from the temperature dependence of DC resistivity and Hall coefficient.

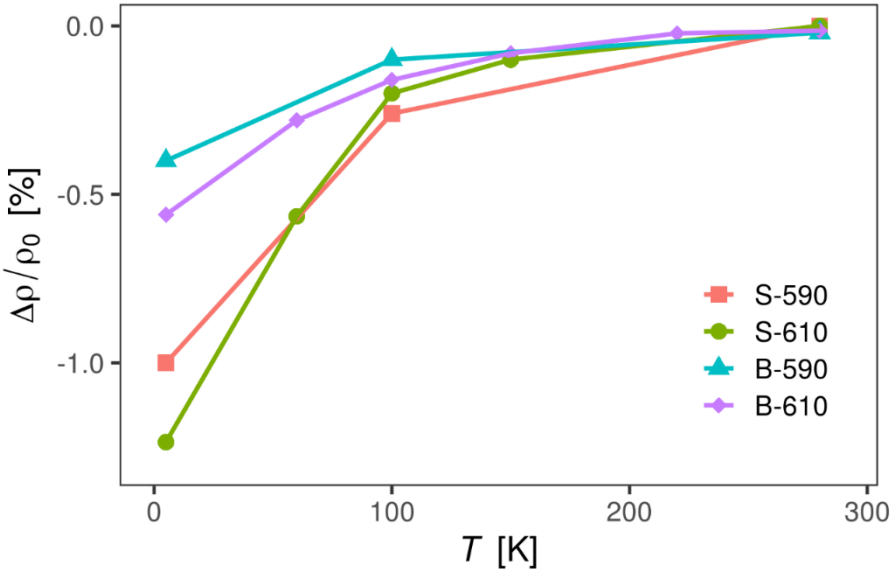

Figure 9 Magnetoresistance for SnO_2 single-layer and bi-layer samples.

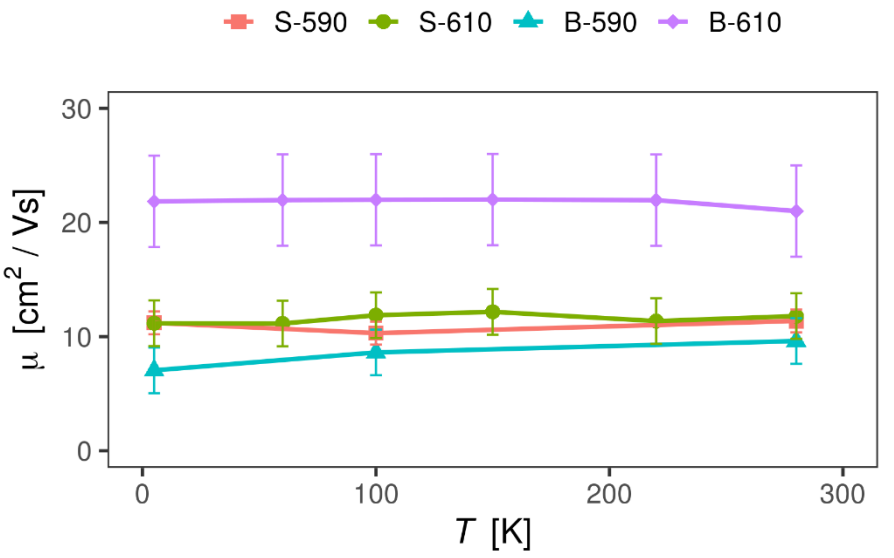

Figure 10 Electron mobility for SnO_2 single-layer and bi-layer samples.

Figure 10 shows the temperature dependence of mobility μ calculated as $\mu = R_H/\varrho$ for all samples. As expected, like the DC resistivity and R_H, the mobility is also temperature-independent, in contrast with simple metallic behavior where mobility and consequently resistivity decreases with decreasing temperature due to electron-phonon scattering.

There are several possible scattering mechanisms that limits transport properties in SnO_2 thin films: scattering on phonons, scattering on ionized impurities provided by intrinsic and extrinsic doping and scattering on neutral defects (crystal imperfections, neutral impurities, grain boundaries …). According to theory only scattering on neutral defects is temperature independent and therefore

Preprints (www.preprints.org) | NOT PEER-REVIEWED | Posted: 8 October 2020 doi:10.20944/preprints202010.0183.v1

presents the dominant scattering mechanism in our samples. The two single-layer (undoped) samples (S-590 and S-610) have practically the same mobility of about 10 cm^2/V, which means that small variation in deposition temperature does not influence mobility. On the other hand, the two bi-layer (doped) samples (B-590 and B-610) show mobility difference of about factor 3. The B-590 sample has even slightly smaller mobility than the undoped samples, but the B-610 sample has a significantly greater mobility. Bi-layer samples are doped with equal fluoride concentrations which would mean that the structural properties related to deposition temperature at least for doped samples, strongly affects the scattering of free carriers.

From Table 2 can be seen that bi-layer samples have larger textured coefficient for (200) orientation. Comparing mobility values to preferred orientation present in sample (Figure 11) it can be observed that mobility increases with increase of (200) texture coefficient. The same relation of mobility to texture coefficient was observed in ref. [28] . The mobility of sample B-590 is smaller than expected and this confirms that crystal orientation is not the only parameter that influences mobility but is the dominant one in our case.

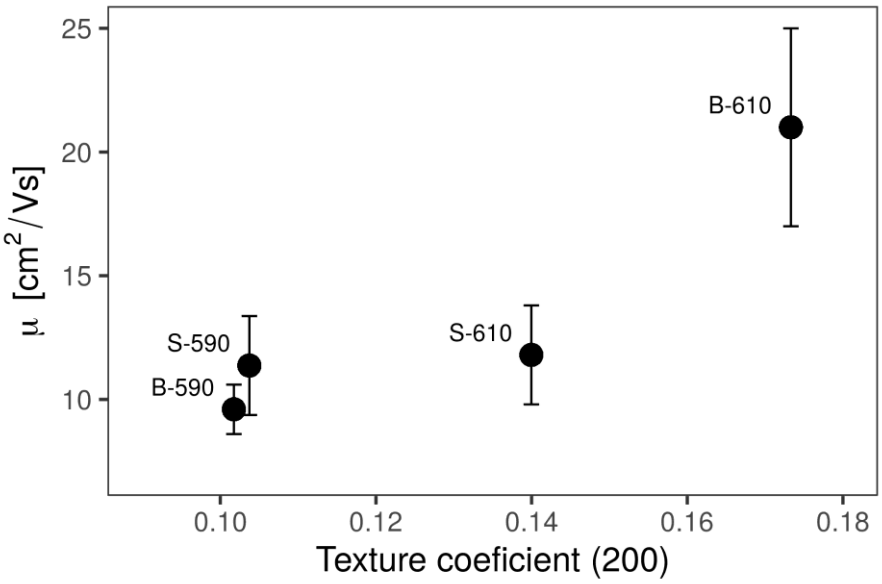

Figure 11 Mobility at 280 K versus preferred crystal orientation.

Mobility dependence on nanocrystal size is not observed. As explained in ref. [28] scattering at nanocrystal boundaries affects mobility only if the nanocrystal size is close to the mean free path of the charge carriers. Estimated mean free path for this type of samples (< 5 nm) is considerably shorter than the nanocrystal sizes of the present films (tens to fifty nanometres). Therefore, Hall mobility is unlikely to be limited by the nanocrystal boundary scattering.

4. Conclusions

We have examined transport properties of SnO_2 thin films deposited by APCVD. Two different type of samples were deposited: undoped SnO_2 single-layer and doped/undoped SnO_2 bi-layer at two different deposition temperatures. Small variation in deposition parameters results in samples with different structural (nanocrystal size and preferred orientation) and transport properties (resistivity and mobility). Results of impedance spectroscopy and Hall probe suggest that transport properties of prepared SnO_2 thin film samples are dominated by scattering at neutral defects. Mobility dependence on preferred orientation presented in samples is observed.

Author Contributions: K. Juraić: samples, preparation, GIXRD experiments and data analysis, writing—original draft preparation, visualization; Z. Siketić: TOF-ERDA experiment and data analysis; M. Čulo and Ž. Rapljenović: Hall probe experiment and analysis; L. Pavić: impedance spectroscopy experiment and data analysis; Mario Bohač: SEM experiments and data analysis; Aden Hodzic, Jasper Rikkert Plaisier: GIXRD experiment, D. Gracin: conceptualization, samples preparation;.

Funding: This research was supported by European Regional Development Fund (ERDF) under the (IRI) project "Improvement of solar cells and modules through research and development" (grant number KK.01.2.1.01.0115) and Croatian Science Foundation Project No. IP-2018-01-5246 and No. IP-2013-11-1011 (magnetotransport experiment).

Acknowledgments: We acknowledge Elettra Sincrotrone Trieste for providing access to its synchrotron radiation facilities (MCX beamline). M. Čulo and Ž. Rapljenović thank Đ. Drobac for cutting the samples for Hall bar geometry and B. Radatović for providing a sample holder and helping with high temperature measurements used to verify temperature trend of resistivity above the room temperature.

Conflicts of Interest: The authors declare no conflict of interest.

References

1. Afre, R.A.; Sharma, N.; Sharon, M.; Sharon, M. Transparent Conducting Oxide Films for Various Applications: A Review. *REVIEWS ON ADVANCED MATERIALS SCIENCE* **2018**, *53*, 79–89.
2. Exarhos, G.J.; Zhou, X.-D. Discovery-based design of transparent conducting oxide films. *Thin Solid Films* **2007**, *515*, 7025–7052.
3. Hosono, H.; Ueda, K. Transparent Conductive Oxides. In *Springer Handbook of Electronic and Photonic Materials*; Kasap, S., Capper, P., Eds.; Springer International Publishing: Cham, 2017; pp. 1–1 ISBN 978-3-319-48931-5.
4. *Handbook of mineralogy*; Anthony, J.W., Ed.; Mineral Data Pub: Tucson, Ariz, 1990; ISBN 978-0-9622097-0-3.
5. Chen, Z.; Pan, D.; Li, Z.; Jiao, Z.; Wu, M.; Shek, C.-H.; Wu, C.M.L.; Lai, J.K.L. Recent Advances in Tin Dioxide Materials: Some Developments in Thin Films, Nanowires, and Nanorods. *Chem. Rev.* **2014**, *114*, 7442–7486.
6. Aliano, A.; Cicero, G.; Nili, H.; Green, N.G.; García-Sánchez, P.; Ramos, A.; Lenshof, A.; Laurell, T.; Qi, A.; Chan, P.; et al. Atmospheric Pressure Chemical Vapor Deposition (APCVD). In *Encyclopedia of Nanotechnology*; Bhushan, B., Ed.; Springer Netherlands: Dordrecht, 2012; pp. 146–146 ISBN 978-90-481-9750-7.
7. Calnan, S.; Tiwari, A.N. High mobility transparent conducting oxides for thin film solar cells. *Thin Solid Films* **2010**, *518*, 1839–1849.
8. Djerdj, I.; Gracin, D.; Juraić, K.; Meljanac, D.; Bogdanović-Radović, I.; Pletikapić, G. Structural analysis of monolayered and bilayered SnO2 thin films. *Surface and Coatings Technology* **2012**, *211*, 24–28.
9. Gordon, R. Chemical vapor deposition of coatings on glass. *Journal of Non-Crystalline Solids* **1997**, *218*, 81–91.
10. Volintiru, I.; de Graaf, A.; van Deelen, J.; Poodt, P. The influence of methanol addition during the film growth of SnO2 by atmospheric pressure chemical vapor deposition. *Thin Solid Films* **2011**, *519*, 6258–6263.
11. Rebuffi, L.; Plaisier, J.R.; Abdellatief, M.; Lausi, A.; Scardi, P. MCX: a Synchrotron Radiation Beamline for X-ray Diffraction Line Profile Analysis: MCX: a Synchrotron Radiation Beamline. *Zeitschrift für anorganische und allgemeine Chemie* **2014**, *640*, 3100–3106.
12. Henke, B.L.; Gullikson, E.M.; Davis, J.C. X-Ray Interactions: Photoabsorption, Scattering, Transmission, and Reflection at E = 50-30,000 eV, Z = 1-92. *Atomic Data and Nuclear Data Tables* **1993**, *54*, 181–342.
13. Siketić, Z.; Radović, I.B.; Jakšić, M. Development of a time-of-flight spectrometer at the Ruder Bošković Institute in Zagreb. *Nuclear Instruments and Methods in Physics Research Section B: Beam Interactions with Materials and Atoms* **2008**, *266*, 1328–1332.

14. Wurst, J.C.; Nelson, J.A. Lineal Intercept Technique for Measuring Grain Size in Two-Phase Polycrystalline Ceramics. *J American Ceramic Society* **1972**, *55*, 109–109.
15. Matsui, Y.; Mitsuhashi, M.; Yamamoto, Y.; Higashi, S. Influence of alcohol on grain growth of tin oxide in chemical vapor deposition. *Thin Solid Films* **2007**, *515*, 2854–2859.
16. Matsui, Y.; Mitsuhashi, M.; Goto, Y. Early stage of tin oxide film growth in chemical vapor deposition. *Surface and Coatings Technology* **2003**, *169–170*, 549–552.
17. Ghoshtagore, R.N. Mechanism of CVD Thin Film SnO[sub 2] Formation. *J. Electrochem. Soc.* **1978**, *125*, 110.
18. Gražulis, S.; Daškevič, A.; Merkys, A.; Chateigner, D.; Lutterotti, L.; Quirós, M.; Serebryanaya, N.R.; Moeck, P.; Downs, R.T.; Le Bail, A. Crystallography Open Database (COD): an open-access collection of crystal structures and platform for world-wide collaboration. *Nucleic Acids Research* **2012**, *40*, D420–D427.
19. Shanthi, S.; Anuratha, H.; Subramanian, C.; Ramasamy, P. Effect of fluorine doping on structural, electrical and optical properties of sprayed SnO2 thin films. *Journal of Crystal Growth* **1998**, *194*, 369–373.
20. Barrett, C. *Structure of metals.*; Horney Press: Place; ISBN 978-1-4437-3140-9.
21. Williamson, G.K.; Hall, W.H. X-ray line broadening from filed aluminium and wolfram. *Acta Metallurgica* **1953**, *1*, 22–31.
22. Kaiser, N. Review of the fundamentals of thin-film growth. *Appl. Opt.* **2002**, *41*, 3053--3060.
23. Arstila, K.; Julin, J.; Laitinen, M.I.; Aalto, J.; Konu, T.; Kärkkäinen, S.; Rahkonen, S.; Raunio, M.; Itkonen, J.; Santanen, J.-P.; et al. Potku – New analysis software for heavy ion elastic recoil detection analysis. *Nuclear Instruments and Methods in Physics Research Section B: Beam Interactions with Materials and Atoms* **2014**, *331*, 34–41.
24. Schiettekatte, F. Fast Monte Carlo for ion beam analysis simulations. *Nuclear Instruments and Methods in Physics Research Section B: Beam Interactions with Materials and Atoms* **2008**, *266*, 1880–1885.
25. Fritzsche, H.; Lark-Horovitz, K. Electrical Properties of p -Type Indium Antimonide at Low Temperatures. *Phys. Rev.* **1955**, *99*, 400–405.
26. Woods, J.F.; Chen, C.Y. Negative Magnetoresistance in Impurity Conduction. *Phys. Rev.* **1964**, *135*, A1462–A1466.
27. Sasaki, W. Negative Magnetoresistance in the Metallic Impurity Conduction of n-Type Germanium. *J. Phys. Soc. Jpn.* **1965**, *20*, 825–833.
28. Wang, J.T.; Shi, X.L.; Liu, W.W.; Zhong, X.H.; Wang, J.N.; Pyrah, L.; Sanderson, K.D.; Ramsey, P.M.; Hirata, M.; Tsuri, K. Influence of Preferred Orientation on the Electrical Conductivity of Fluorine-Doped Tin Oxide Films. *Sci Rep* **2015**, *4*, 3679.